Island Arc

Island Arc (2010) 19, 134–150

Research Article

Geophysical implications of Izu–Bonin mantle wedge hydration from chemical geodynamic modeling

LAURA B. HEBERT* AND MICHAEL GURNIS

California Institute of Technology, Pasadena, CA 91125, USA

Abstract Using two-dimensional dynamic models of the Northern Izu–Bonin (NIB) subduction zone, we show that a particular localized low-viscosity ($\eta_{LV} = 3.3 \times 10^{19} - 4.0 \times 10^{20}$ Pa s), low-density ($\Delta\rho \sim -10$ kg/m^3 relative to ambient mantle) geometry within the wedge is required to match surface observations of topography, gravity, and geoid anomalies. The hydration structure resulting in this low-viscosity, low-density geometry develops due to fluid release into the wedge within a depth interval from 150 to 350 km and is consistent with results from coupled geochemical and geodynamic modeling of the NIB subduction system and from previous uncoupled models of the wedge beneath the Japan arcs. The source of the fluids can be either subducting lithospheric serpentinite or stable hydrous phases in the wedge such as serpentine or chlorite. On the basis of this modeling, predictions can be made as to the specific low-viscosity geometries associated with geophysical surface observables for other subduction zones based on regional subduction parameters such as subducting slab age.

Key words: geoid, gravity, GyPSM-S, Izu–Bonin, low-viscosity channel, topography.

INTRODUCTION

Convergent margin volcanism can be explained in terms of the addition of volatiles from the dehydrating slab to the overlying mantle wedge, leading to water-fluxed melting. The locations of dehydration reactions within the slab are dependent on the thermal structure, which is defined primarily by the age of the plate. Infiltration and equilibration of hydrous fluids with the wedge peridotite allow for increasing amounts of water to be stabilized in nominally anhydrous minerals (NAM) such as olivine, garnet, orthopyroxene, and clinopyroxene (Bell & Rossman 1992), as well as for the appearance of hydrous phases such as amphibole, antigorite, chrysotile, and chlorite (Davies & Stevenson 1991; Iwamori 1998; Grove *et al.* 2006; Kawakatsu & Watada 2007). The effect of increasing water content in NAM is twofold: (i) decreasing solidus temperatures (Gaetani & Grove 2003; Asimow *et al.* 2004) and (ii) water-weakening that reduces the viscosity of the solid material (Hirth & Kohlstedt 1996). As such, there is a dual effect of hydrous fluid introduction on the geochemistry of initial melts within the system and on the force balance within the wedge.

Previous modeling studies (Davies & Stevenson 1991; Iwamori 1998; Gerya & Yuen 2003; Arcay *et al.* 2005) have addressed the role of water and wedge hydration in the subduction system together with dynamical considerations, emphasizing the role of hydrous minerals in acting as transport agents and/or sources of water, and using phase diagram parameterizations to approximate the chemical variables within the system. Recent work (Iwamori 2007; Tonegawa *et al.* 2008) has further underscored the importance of the hydration of NAM in the subduction wedge, and the implications for deep transport of hydrated material. Additionally, a coupled approach, which includes self-consistent treatments of melting, water stability in hydrous and nominally anhydrous phases, water-weakening, and a change in bulk composition due to melting, has been

*Correspondence: University of Maryland, College Park, MD 20742, USA (email: lhebert@geol.umd.edu).

Received 16 August 2008; accepted for publication 16 March 2009.

doi:10.1111/j.1440-1738.2009.00688.x

introduced. Geodynamic and Petrological Synthesis Model for Subduction (GyPSM-S) (Hebert *et al.* 2009) involves iterative interaction between ConMan, a 2D thermal and variable viscosity numerical flow model (King *et al.* 1990), and pHMELTS, a thermodynamic energy minimization algorithm that can calculate water partitioning into NAM (Ghiorso & Sack 1995; Asimow *et al.* 2004; Smith & Asimow 2005). The significance of the coupled scheme is the detailed tracking of fluids and their rheological and chemical effects from release to initiation of melting. The primary results of the GyPSM-S models demonstrate the existence of a low-viscosity channel (LVC) within the mantle wedge, the process by which LVCs form, and the limitations on LVC geometry (Hebert *et al.* 2009).

The LVC, as defined by Hebert *et al.* (2009), is effectively a zone of water saturation that develops immediately adjacent to the subducting slab, consisting of hydrous phases and NAM with high water contents (water solubility increases with pressure, and can approach thousands of ppm at depth when all NAM phases are considered). The thickness of the zone is limited at the base by the subducting plate and at the top by the spatial position of the water-saturated peridotite solidus within the wedge (melt initiation) (Hebert *et al.* 2009). First-order controls on the geometry of hydration within the wedge arise from the thermal structure of the down-going slab (mostly a function of slab age), slab dip angle, mechanism of fluid transport within the wedge, and spatial position of the water-saturated solidus within the wedge (Hebert *et al.* 2009). Thus, variations in the geometry of the LVC from model to model, for example from a relatively thin, uniform channel to a larger wedge, depend on parameters specifically affecting the thermal structure within the wedge and the intensity and location of fluid sources along the slab (Hebert *et al.* 2009). Whilst the mechanisms that lead to the localized low-viscosity geometry and the control over its shape are well understood through an examination by a coupled model, other studies have led to similar conclusions as to the existence of low-viscosity zones in the mantle wedge. Results from both Iwamori (2007) and Tonegawa *et al.* (2008) show localized potential low-viscosity regions within the mantle wedge beneath the Japan arcs, comparable to results from Hebert *et al.* (2009). Ultimately, understanding the development and shape of LVCs is important for considering the initiation of melting within the wedge (Hebert *et al.* 2009), the state of stress within the wedge (Billen & Gurnis 2001), for changing slab dip angle (Manea & Gurnis 2007), as well as for transport of hydrated, relatively fertile near-slab material into the deep mantle (Schmidt & Poli 1998; Dixon *et al.* 2002; Le Roux *et al.* 2002; Cooper *et al.* 2004; Donnelly *et al.* 2004; Iwamori 2007; Kawakatsu & Watada 2007; Tonegawa *et al.* 2008).

The influence of the existence of localized low-viscosity geometries within the wedge on the overall flow field and force balance can be examined through surface observations particular to the viscosity structure, such as dynamic topography and gravity and geoid anomalies (Billen & Gurnis 2001, 2003). The geoid represents a combination of contributions from internal density variations (thermal, mineralogical) and from boundary deformations induced by the flow field (Davies 1981; Hager 1984). Subduction zones can be characterized by long-wavelength (10^3–10^4 km) geoid highs over slabs, and shorter wavelength (10^2 km) geoid lows over trenches (Zhong & Gurnis 1992; Billen *et al.* 2003). Long-wavelength geoid highs are interpreted as indicative of a radial viscosity structure where the viscosity of the upper mantle (η_{UM}) is less than the viscosity of the lower mantle (η_{LM}) leading to regional compensation of subducting slabs (Hager 1984; Moresi & Gurnis 1996). However, shorter-wavelength geoid anomalies and the depth of back-arc basins may be resolved by studying viscosity variations caused by thermal or compositional variations within the upper mantle (Billen *et al.* 2003). Numerical models have demonstrated that stresses are transmitted through viscous coupling in the wedge from the subducting slab to the overlying lithosphere (Sleep 1975; Zhong & Gurnis 1992; Zhong *et al.* 1998). Billen and Gurnis (2001) demonstrated that a localized region of low viscosity within the upper mantle rather than an overall change in asthenospheric viscosity was required to match the topography and geoid signal on the overlying plate, as a reduction in wedge viscosity reduces the coupling between the slab and the overlying plate, resulting in a less negative dynamic topography. Billen and Gurnis (2003) then successfully investigated the relative sizes and shapes of low-viscosity, low-density regions necessary to match signals in the Tonga–Kermadec and Central Aleutian subduction zones. While it is thus well understood that localized low-viscosity regions may be important to the force balance within mantle wedges, the mechanisms of development of these regions and how the regional geometries change based on changing

subduction behaviors have only recently been established (Tonegawa *et al.* 2008; Hebert *et al.* 2009). The next logical step would be to construct models that include localized low-viscosity structures to attempt to match observed geophysical signals in a particular locality to evaluate previous results from coupled modeling (Hebert *et al.* 2009) and other modeling studies (Iwamori 2007; Tonegawa *et al.* 2008).

Accordingly, in this study, we model geophysical signals (geoid and gravity anomalies, topography) from the northern Izu–Bonin subduction (NIB) system (32°N, ~136–146°E). We evaluated the impact of potential localized low-viscosity geometries, including a regional result (NIB) from GyPSM-S (Hebert *et al.* 2009), by matching model results to actual datasets. We demonstrate that the particular structure solved by GyPSM-S is most appropriate, thus matching geophysical observables with a particular hydration structure developed through a coupled model. Notably, the geometry of the preferred structure also agrees with modeling results from Tonegawa *et al.* (2008), using receiver functions.

The northern Izu–Bonin subduction system can be described by the descent of relatively old (*ca* 135 Ma) Pacific lithosphere beneath the younger Philippine Sea Plate at a moderate convergence velocity of around 5.0 cm/y, and a convergence angle of 45° (Fig. 1) (Stern *et al.* 2003). The Izu–Bonin arc crust between the Izu–Bonin Trench and the Shikoku Basin is relatively thin (~20 km), and is defined by a narrow (~300 km wide) topographic high over the arc of about 3 km with an associated gravity high of about 100 mGal. The trench is defined by a topographic low of about 3 km and a gravity low of about 280 mGal. Seismic investigation has determined a velocity structure that can be interpreted as different lithological layers within the arc crust (Suyehiro *et al.* 1996; Takahashi *et al.* 1998, 2007; Kitamura *et al.* 2003), most notably a middle crustal layer with P-wave

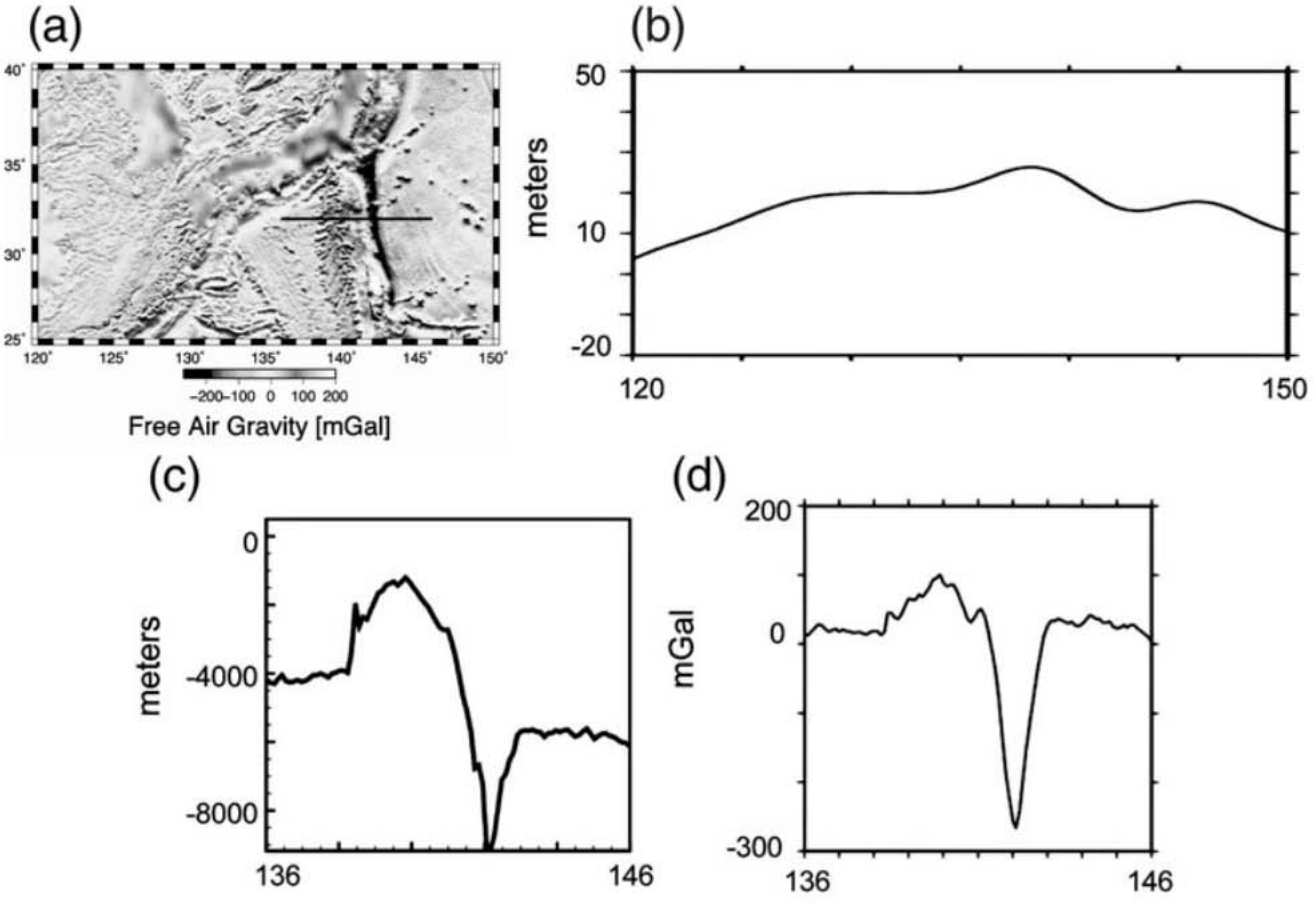

Fig. 1 (a) Observed free air gravity for the northern Izu–Bonin region (Sandwell & Smith 1997), (b) geoid east–west profile extracted from EGM96 dataset (Lemoine **et al.** 1998) using terms from degree and order 2–70 (note the x-scale extends from 120° to 150°E to show long-wavelength features), (c) east–west bathymetric profile extracted from the GMRT dataset (Arko **et al.** 2007) across 32°N, which does not vary appreciably from actual bathymetry, and (d) free air gravity anomaly east–west profile extracted from dataset of Sandwell and Smith (1997) (version 15.1).

velocities approximating mean continental crustal velocities (6.4 km/s, Christensen & Mooney 1995). To the west of the arc (Shikoku Back-Arc Basin), and to the east of the trench (Pacific Plate), the oceanic crust is uniformly about 8 km in thickness (Takahashi *et al.* 1998). The relative offset in the bathymetry on either side of the arc–trench area is due to the difference in ages of the two converging oceanic plates. The geoid, filtered from degree and order 2–70, is described by a broad high over the arc complemented by a low over the trench. The close proximity of the Ryukyu Trench and Arc to the west leads to a somewhat lower amplitude high and a general decrease towards the west. Altogether, the change in height of the geoid is about 20 meters. Seismicity within the slab extends to depths of about 475 km, and there is seismic evidence for flattening of the slab within the transition zone (Van der Hilst *et al.* 1991; Fukao *et al.* 1992; Widiyantoro *et al.* 1999; Fukao *et al.* 2001; Gorbatov & Kennett 2003).

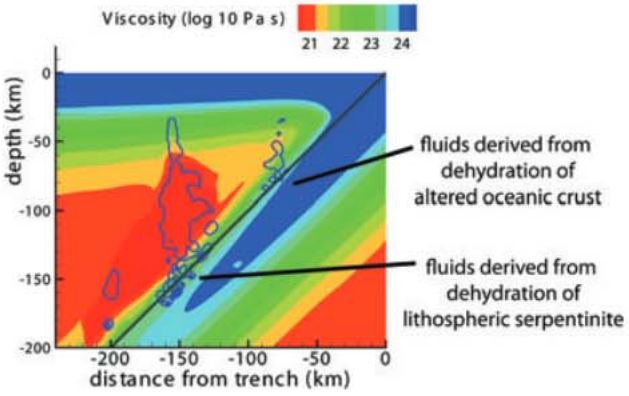

Fig. 2 GyPSM-S results for the viscosity structure of the shallow (< 200 km) mantle wedge for the Northern Izu–Bonin model calculation showing the influence of the high water contents in nominally anhydrous minerals as a localized zone of viscosity reduction. The geometry of the low-viscosity region is directly influenced by the vertical migration of water from the dehydrating subducting slab (shown as blue lines), the majority of which is released at depths ≤ 150 km from the lithospheric serpentinite layer. (For interpretation of the references to color in this figure legend, refer to the web version of the article).

METHODS

MODEL LOW-VISCOSITY ZONE GEOMETRIES

A number of studies (Billen & Gurnis 2001, 2003; Honda & Saito 2003; Honda *et al.* 2007; Manea & Gurnis 2007) have introduced the potential dynamic impact of low-viscosity regions (due to water from the slab interacting with the wedge peridotite) within the mantle wedge using parameterized low-viscosity geometries in numerical models. These geometries range in lateral extent from a thin, uniform channel adjacent to the downgoing slab to a large structure that encompasses the 'wedge' from the slab to the back-arc. The extent to which the viscosity is lowered relative to the ambient mantle varies among models, but is based on a constant reduction factor (Billen & Gurnis 2001; Honda & Saito 2003).

The GyPSM-S model (see Hebert *et al.* 2009, for a complete model description) characterized the shallow wedge structure (<200 km depth) for the NIB system (Fig. 2), showing the development of the hydrated wedge due to the subduction of a mature slab at a moderately slow convergence velocity. Low- to mid-pressure fluid releases are dominantly from the altered oceanic crust (AOC) layers (from increasing depths into the slab), and strong, high-pressure fluid release that originates in the lithospheric serpentinite slab layer (Hebert *et al.* 2009). The fluid release from the serpentinite layer results in a continuous cooling of the melting region, due to the effects of latent heat of melting, culminating in a vertical retreat of the water-saturated solidus into the wedge, and a lengthening of the deeply-originating fluid transport pathway (Hebert *et al.* 2009). This leads to the development of a long hydration corridor through the wedge (Hebert *et al.* 2009). Ultimately, with advection, the hydrated region approaches the shape of a wedge at shallower depths and a channel at greater depths [noted as 'extended' low-viscosity channel, (ELVC)], where the left boundary of the hydrated geometry is controlled by the deepest location of fluid release from the slab, assuming a vertical fluid trajectory. This particular shape is in contrast to the uniformly thick LVCs associated with the subduction of relatively younger slabs, or when the slab dip angle is steeper, resulting in narrowing of the region of fluid infiltration into the wedge (Hebert *et al.* 2009). Tonegawa *et al.* (2008) used radial and transverse receiver functions to characterize the seismological structure of the upper mantle beneath Japan, determining the distribution of water in and above the subducting slab through numerical simulations. The study resulted in an interpretation for the shape of the hydrated envelope within the mantle wedge, including water in NAM and hydrated phases, that closely approximates the solution of GyPSM-S for the Izu–Bonin region (ELVC).

Thus, given the possible solutions for the geometry of a low-viscosity region beneath the Izu–

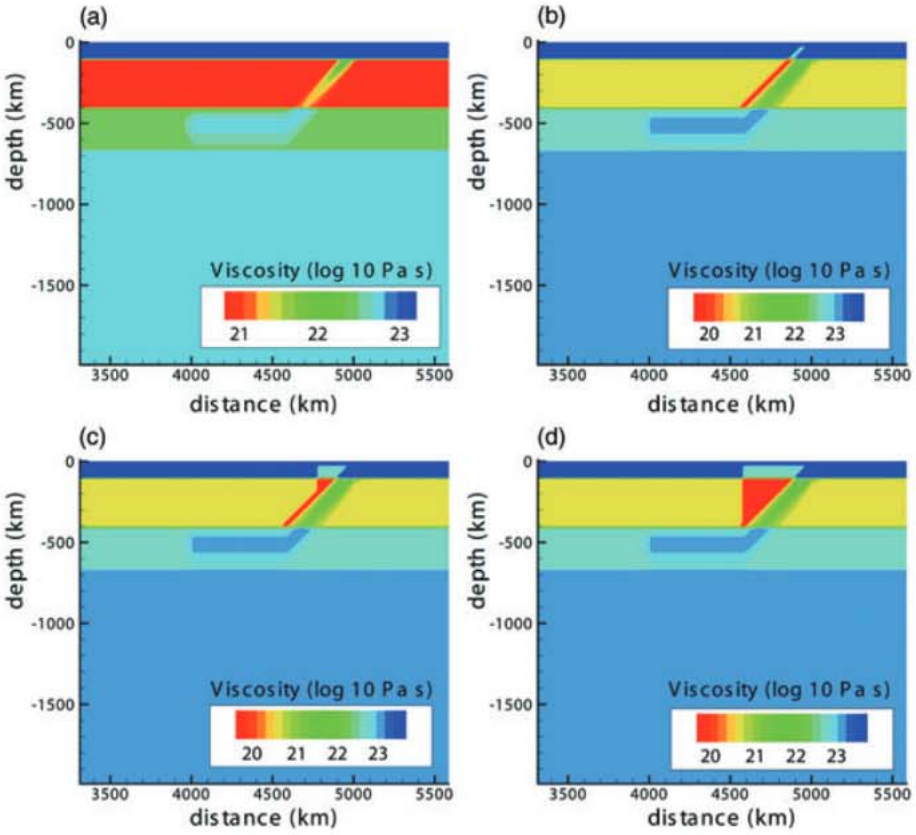

Fig. 3 Model viscosity structure with addition of parameterized low-viscosity (LV) regions. (a) No (LV), corresponds to a lack of an imposed low-viscosity zone, (b) low-viscosity channel (LVC), corresponding to a slab-adjacent uniform 50 km thick LVC that extends to the top of the transition zone, or where the slab begins to flatten (note change in viscosity scale), (c) 'extended' LVC (ELVC), approximating a wedge geometry in the shallow regions of the mantle wedge, but remaining a uniform channel at greater depths due to the near slab-parallel flow field, and (d) low-viscosity wedge (LVW), corresponding to a full 'wedge'-type geometry. (For interpretation of the references to color in this figure legend, refer to the web version of the article).

Bonin Arc, we choose three potential geometries to include in our modeling along with the possibility of an absent low-viscosity structure (Fig. 3a): (i) a uniform-thickness LVC (Fig. 3b); (ii) an ELVC (Fig. 3c) akin to the regional solution for Izu–Bonin from GyPSM-S (Hebert *et al.* 2009) and for Japan (Tonegawa *et al.* 2008); and (iii) a low-viscosity wedge (LVW, Fig. 3d) in the manner of Billen and Gurnis (2001) and Honda *et al.* (2007). Assuming vertical fluid transport, it is the interplay between the slab dip angle and the deepest location of slab fluid release that determines the lateral extent of the wedge geometry. The tops of these low-viscosity regions are defined by the base of the conductive layer within the overriding plate, and the regions extend to where the slab flattens in the transition zone. The hydrated NAM can transport water to great depths (Iwamori 2007; Tonegawa *et al.* 2008; Hebert *et al.* 2009), the basis for the theoretical continuation of the LVC to the transition zone.

Density variations produced by the GyPSM-S calculation for the low-viscosity regions relative to ambient nominally anhydrous mantle wedge are about $\Delta\rho \sim -50$ to -20 kg/m^3. However, previous modeling (Billen & Gurnis 2003) investigated the range $\Delta\rho \sim -50$ to 0 kg/m^3, and we therefore include this range in the geophysical modeling for completeness (Table 1).

MODEL CONSTRUCTION

We construct an uncoupled model for calculation of topography and geoid and gravity anomalies using ConMan (Fig. 4a) (King *et al.* 1990). A penalty formulation is used to enforce incompressibility in the solution of the momentum equation (King *et al.* 1990). The dynamics are controlled by conservation equations of mass, momentum, and energy, with the Boussinesq approximation. The non-dimensional equations for mass and momentum are:

$$\nabla \cdot \mathbf{v} = 0 \quad \text{and} \tag{1}$$

$$-\nabla P + \nabla \cdot (\eta \dot{\varepsilon}) = Ra T \hat{k}, \tag{2}$$

where v is the dimensionless velocity, T is the dimensionless temperature, P is the dimensionless pressure, η is dimensionless viscosity, and $\hat{k}$ is a unit vector in the direction of gravity. The dimensionless Rayleigh number combines all the material properties:

Table 1 Summary of low-viscosity region model cases

Model	Depth extent of channel section (km)	Depth extent of wedge section (km)	Width of channel from top of slab (km)	Width of wedge at top (km)	Average water content in olivine (ppm)	Δρ (LVZ-wedge) (kg/m^3)
no LV	na	na	na	na	na	na
LVC1	400	0	50	0	1000	0
LVC2	400	0	50	0	1000	–10
LVC3	400	0	50	0	1000	–20
LVC4	400	0	50	0	1000	–50
ELVC1	400	100	50	100	1000	0
ELVC2	400	150	50	150	1000	0
ELVC3	400	180	50	180	1000	0
ELVC4	400	200	50	200	1000	0
ELVC5	400	200	50	200	2000	0
ELVC6	400	200	50	200	1000	–10
ELVC7	400	200	50	200	1000	–20
ELVC8	400	200	50	200	1000	–50
ELVC9	400	100	50	100	1000	–10
ELVC10	400	100	50	100	1000	–20
ELVC11	400	100	50	100	1000	–50
ELVC12	400	150	50	150	1000	–10
ELVC13	400	150	50	150	1000	–20
ELVC14	400	150	50	150	1000	–50
ELVC15	400	180	50	180	1000	–10
ELVC16	400	180	50	180	1000	–20
ELVC17	400	180	50	180	1000	–50
LVW1	400	300	50	300	1000	0
LVW2	na	400	na	400	1000	0
LVW3	400	300	50	300	1000	–10
LVW4	400	300	50	300	1000	–20
LVW5	400	300	50	300	1000	–50
LVW6	na	400	na	400	1000	–10
LVW7	na	400	na	400	1000	–20
LVW8	na	400	na	400	1000	–50
ELVC18	400	100	50	100	1000	–30
ELVC19	400	100	50	100	1000	–40
ELVC20	400	150	50	150	1000	–30
ELVC21	400	150	50	150	1000	–40
ELVC22	400	200	50	200	1000	–30
ELVC23	400	200	50	200	1000	–40
LVC5	400	0	50	0	1000	–30
LVC6	400	0	50	0	1000	–40
LVW9	400	300	50	300	1000	–30
LVW10	400	300	50	300	1000	–40
LVW11	na	400	na	400	1000	–30
LVW12	na	400	na	400	1000	–40
ELVC24	400	250	50	250	1000	0
ELVC25	400	250	50	250	1000	–10
ELVC26	400	250	50	250	1000	–20
ELVC27	400	250	50	250	1000	–30
ELVC28	400	250	50	250	1000	–40
ELVC29	400	250	50	250	1000	–50
LVW13	400	350	50	350	1000	0
LVW14	400	350	50	350	1000	–10
LVW15	400	350	50	350	1000	–20
LVW16	400	350	50	350	1000	–30
LVW17	400	350	50	350	1000	–40
LVW18	400	350	50	350	1000	–50

Δρ, density difference between low-viscosity zone and ambient mantle wedge; ELVC, 'extended' LVC; na, not applicable; LV, low viscosity; LVC, low-viscosity channel; LVW, low-viscosity wedge.

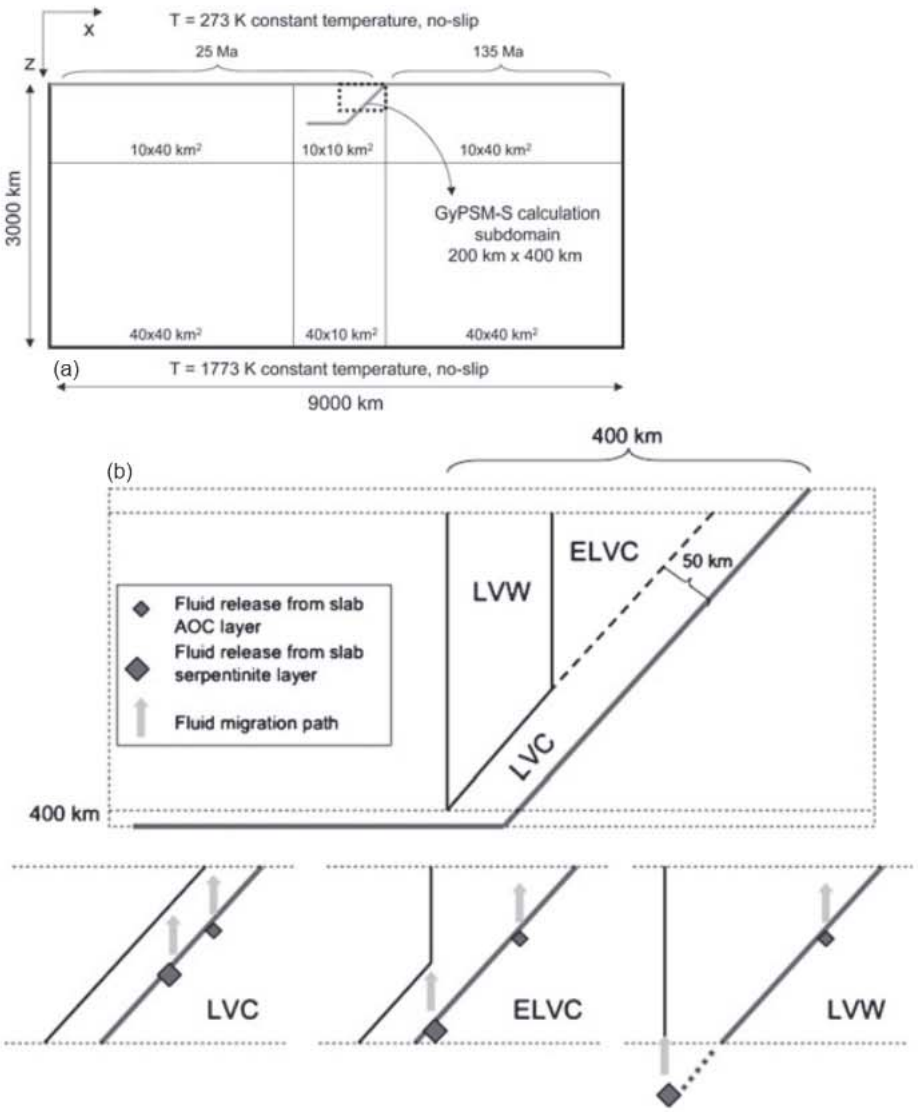

Fig. 4 Uncoupled model setup for calculation of topography, geoid height, and gravity anomalies. (a) Schematic representation of calculation domain, and (b) schematic representation of model geometries in association with fluid release locations. AOC, altered oceanic crust; ELVC, 'extended' LVC; LVC, low-viscosity channel; LVW, low-viscosity wedge.

$$Ra = \frac{g\alpha\Delta T d^3}{\kappa\eta}, \tag{3}$$

where g is the acceleration due to gravity, α is the coefficient of thermal expansion, ΔT is the temperature drop across the box, d is the depth of the box, κ is the thermal diffusivity, and η is the dynamic viscosity (Table 2). The non-dimensional energy equation is:

$$\frac{\partial T}{\partial t} = -\nabla \cdot \nabla T + \nabla^2 T, \tag{4}$$

where t9 is dimensionless time. A streamline upwind Petrov–Galerkin method (Brooks & Hughes 1982) is used to solve Equation 4. The model domain was extended vertically and horizontally in order to account for the long-wavelength features in the geoid signal. The model domain, 9000 km in width, extends from the surface to the core–mantle boundary (3000 km). The refined computational grid consists of 45 000 bilinear quadrilateral elements: 150 in the vertical direction and 300 in the horizontal, and element resolution ranges from (40 km × 40 km) to (10 km × 10 km). A refined zone that includes the shallow mantle wedge has the highest resolution (10 km × 10 km). We do not include a fault (shear zone) interface within the lithosphere along the subduction plate boundary. The initial thermal structures of the subducting slab and of the overlying lithosphere are defined by a half-space cooling model for each plate based on age and the top and bottom surfaces of the model domain have isothermal, no-slip boundary conditions. Analytical corner flow (Batchelor 1967) was used to calcu-

Table 2 Model parameters held constant

Parameter	Value	Units
ΔT	1500	°C
Ra	1.40×10^8	†
η_0	3.0×10^{20}‡	Pa s
Q	500	kJ/mol
$A_{\text{Philippine}}$	24§	My
A_{Pacific}	141§	My
κ	1.0×10^{-6}	m^2/s
α	2.5×10^{-5}	1/K
g	10.0	m/s^2
G	6.67×10^{-11}	Nm^2/kg^2
d	3000	km
R	8.31	J/K mol
$X\text{H}_2\text{O}_{\text{crit}}$	110¶	ppm

† dimensionless quantity.
‡ Billen and Gurnis (2003).
§ Müller *et al.* (1997).
¶ Hebert *et al.* (2009).

$A_{\text{Philippine}}$, age of the Philippine oceanic lithosphere in My; A_{Pacific}, age of the Pacific oceanic lithosphere in My; α, coefficient of thermal expansion; d, depth of the box; g, gravity; G, gravitational constant; κ, thermal diffusivity; LVZ, low viscosity zone; η_0, reference viscosity; R, gas constant; Ra, Rayleigh number; Q, activation energy; ΔT, temperature drop across the box; $X\text{H}_2\text{O}_{\text{crit}}$, critical value for water weakening.

late the initial evolution of the thermal field and the thermal structure for the wedge is determined by solving the advection–diffusion equation (Eqn 4) with the fixed flow field to steady-state. Instantaneous flow is driven by internal thermal and chemical buoyancy forces. The slab contributes the primary thermal variation. Imposed chemical heterogeneities such as crustal layering, mineralogical phase transformations, and variations in the degree of wedge hydration are introduced as density variations and represent sources of buoyancy. The slab velocities are kinematically imposed and slab dip in the upper mantle is a constant 45°, with a flattening to near-horizontal within the transition zone (Van der Hilst *et al.* 1991; Fukao *et al.* 1992; Widiyantoro *et al.* 1999; Fukao *et al.* 2001; Gorbatov & Kennett 2003).

INTERNAL DENSITY VARIATIONS AND BACKGROUND RADIAL VISCOSITY

The area of interest is restricted to the Izu–Bonin Trench, the arc edifice and oceanic crust immediately to the west and east (~136–146°E). We do not account for additional structures further to the west and east in the extended model domain. A lower density island arc could contribute to topographic and gravity highs (Sleep 1975; Zhong & Gurnis 1994). Therefore, we include low-density crustal layering in the models. Arc crustal structure is defined by density anomalies interpreted from seismic velocities from the Shikoku Basin to the Izu–Bonin Trench (Suyehiro *et al.* 1996; Takahashi *et al.* 1998). The across-arc variation in the crustal structure in the NIB system is distinguished by the presence of three layers: (i) upper crust interpreted as sediments and basalts with velocities that increase with depth from 1.5 to 5.6 km/s over 5 km; (ii) middle crust with P-wave velocities of 6.1–6.3 km/s, corresponding to intermediate (andesitic to tonalitic) plutonic rocks that are close to the mean velocity of continental crust (~6.4 km/s, Christensen & Mooney 1995); and (iii) thick lower crust with P-wave velocities of 7.1–7.3 km/s, interpreted as gabbroic igneous underplating (Takahashi *et al.* 1998). The arc crustal thickness varies from 18 km below the forearc to 20 km beneath the central rift zone 260 km from the trench (Takahashi *et al.* 1998).

The crustal structure of the subducting Pacific Plate is about 8 km thick, and can be subdivided into three layers: (i) upper crustal layer with two defining velocity characteristics (upper layer with P-wave velocities ranging 1.6–1.8 km/s, lower layer with velocities of 3.0–4.3 km/s); (ii) middle layer with velocities of 4.7–5.7 km/s; and (iii) lower layer with velocities 6.4–6.5 km/s (Takahashi *et al.* 1998). For simplicity, we assume that the crust of the Shikoku Basin is the same as the Pacific Plate. We are somewhat limited by the resolution of the model (10-km vertical increments along the topmost elements) in reconstructing a realistic density structure within the crust; however, we attempt to include the most important density variations despite the restrictions in resolution.

The exothermic phase transformation from olivine to wadsleyite ($\alpha \square \beta$) is represented by a density increase of 7.2% at 410 km depth and the endothermic phase transformation from ringwoodite (γ) to perovskite plus magnesiowüstite is represented by a density increase of 8.4% at 670 km depth (Jeanloz 1989), with deflections of the position of the phase boundary above and below these depths associated with the cold subducting slab. The basalt to eclogite transition within the slab is accounted for by a 6% density increase within the AOC layer of the down-going plate. Despite evidence that including the effects of phase transformations near the transition zone in the calculation of the dynamic topography and the geoid is insignificant considering the overwhelm-

ing effect of the radial viscosity structure (King 2002), we include these effects as part of a comprehensive approach.

The radial background viscosity structure consists of four layers: lithosphere, upper mantle, transition zone, and lower mantle. Viscosity is both temperature- and composition-dependent, with the viscosity in each layer defined with respect to a reference viscosity (η_0) with a value of 3.0×10^{20} Pa s (Billen & Gurnis 2003): upper mantle ($\eta_{UM} = 1 \times \eta_0$), transition zone ($\eta_{TZ} = 100 \times \eta_0$), lower mantle ($\eta_{LM} = 300 \times \eta_0$), and lithosphere (<100 km depth) ($\eta_{LITH} = 1000 \times \eta_0$). The maximum viscosity of the slab at all depths is $1000 \times \eta_0$. Parameterized regions (Fig. 4b) of hydration within the upper mantle are included, where reductions in viscosity within the hydration zones are due to higher concentrations of water in NAM and the superposition of the thermal structure in the wedge. A depth of 400 km is considered a probable maximum for the parameterized hydrated regions in this system because of the flattening of the slab in the transition zone.

CALCULATION OF GEOPHYSICAL SURFACE OBSERVABLES

Calculated topography (h), geoid height (ΔN), and gravity anomalies (Δg) are compared with observations to assess the appropriateness of the viscosity and buoyancy models. We evaluate not only the preferred parameterization that includes an extended LVC region (ELVC) (Tonegawa *et al.* 2008; Hebert *et al.* 2009) but also other models (no LV region, uniform thickness LVC, LVW) (Fig. 3). We additionally evaluate the impact of different degrees of hydration of the low-viscosity zone, leading to different magnitudes of lateral viscosity contrast within the wedge, and we evaluate different magnitudes of density contrast between the hydrated zones and the ambient nominally anhydrous wedge. Similarly to the GyPSM-S model (Hebert *et al.* 2009), we treat water content in olivine as the sole compositional influence on the viscosity law:

$$\eta = \frac{\eta}{\eta_0} = \exp\left[\frac{Q}{RT_0} * \left(\frac{T_0}{T} - 1\right) * \left(\frac{XH_2O}{XH_2O_{crit}}\right)^{-1}\right], \quad (5)$$

where $XH_2O > XH_2O_{crit}$, η_0 is the reference viscosity, Q is the activation energy, R is the gas constant, T_0 is the model reference temperature, XH_2O is the water content in olivine, and XH_2O_{crit} is the critical value for water weakening (Table 2). At upper mantle pressures and temperatures, olivine is the dominant mineral in the solid matrix, and experimental studies have focused on dislocation creep in hydrated olivine aggregates as a mantle proxy (Hirth & Kohlstedt 1996). However, substantial amounts of water can also go into other NAM, such as the pyroxenes and garnet. The viscosity within the hydrated regions (parameterized by an average $XH_2O_{olivine}$) while significantly reduced relative to an anhydrous value, is non-uniform due to the superimposed thermal structure ($\eta_{LV} = 3.3 \times 10^{19}$–$4.0 \times 10^{20}$ Pa s for $XH_2O_{olivine} = 1000$ ppm).

The dynamic topography (h) balances the normal stress on the top surface and becomes:

$$h = \frac{\eta_0 k}{\Delta\rho g d^2} \sigma_z, \quad (6)$$

where σ_z is the non-dimensional stress, $\Delta\rho$ is the density difference across the top of the domain (representing the contrast between lithosphere and water, as we assume the top surface of the domain is covered with water) and d is the depth of the model domain (Table 2). We calculate topography using the consistent boundary flux method (Zhong *et al.* 1993). We match our model topography results with the residual topography, which is the topography that results when the normal subsidence of the oceanic lithosphere is removed from the observed bathymetry (Fig. 1), using:

$$h_T = h_0 - \left(2600 + 220(A)^{1/2}\right) \quad (7)$$

where h_T is the residual depth in meters, A is the age of the oceanic lithosphere in My (Table 2), and h_0 is the observed bathymetry in meters (Schroeder 1984; Pribac 1991). We compute the predicted geoid height in the wavenumber domain and include contributions from topography on the top surface and density anomalies within the model domain, assuming no density anomalies outside the domain (density anomalies within the domain are converted into mass sheets at each layer of nodes within the model, and topography along the top surface is likewise converted to a mass sheet and summed to form the surface response). To account for the difference in model plate ages, the topography is shifted by a mean value along the edge of the domain before computing geoid height. Gravity anomalies are also computed in the wavenumber domain. The gravity and geoid results were both subjected to low bandpass filters in order to attenuate frequencies higher than were represented in the regional datasets.

MODELING RESULTS

TOPOGRAPHY

Incorporation of the low-viscosity region has the primary influence of increasing the topography associated with the arc edifice. Without a low-viscosity region (no LV, Fig. 5e), the calculated topography for the arc is too low and too narrow compared with that observed, and the trench depth is underestimated. When a low-viscosity channel is added (LVC1, Fig. 5f), forearc topography increases to more closely match that observed and trench depth increases to match that observed. The incorporation of the wedge-type structure (ELVC4, Fig. 5g) generates a peak in the arc topography associated with the maximum horizontal extent of the hydrated region in the shallow mantle wedge, more closely matching the amplitude of the observed dataset in that area. Increasing the relative viscosity difference between the ambient mantle wedge and the low-viscosity region by increasing the amount of water in olivine (ELVC5) results in a further increase in the amplitude of the calculated topography by 280 m, and an increase in the trench depth.

Increasing the lateral and depth extent of the ELVC to approach a true wedge (LVW2, Fig. 5h) has a significant influence on the shape of the calculated topography. The lateral extent of the ELVC/LVW corresponds to the deepest point of slab dehydration, assumed to result in a long fluid pathway similar to the NIB GyPSM-S model result (Fig. 2) (Hebert *et al.* 2009). As the lateral extent of the ELVC increases from the nominal LVC width (50 km), the topography changes from a smooth top to one that peaks within the arc, followed by the smooth top again as the increases in calculated topography due to the low-viscosity zone are added away from the highs associated with the arc edifice (Fig. 6a). The peak is caused by the sharp edge to the low-viscosity region that results in a concentration in stress (e.g. Billen *et al.* 2003). Therefore, the highs in the topography

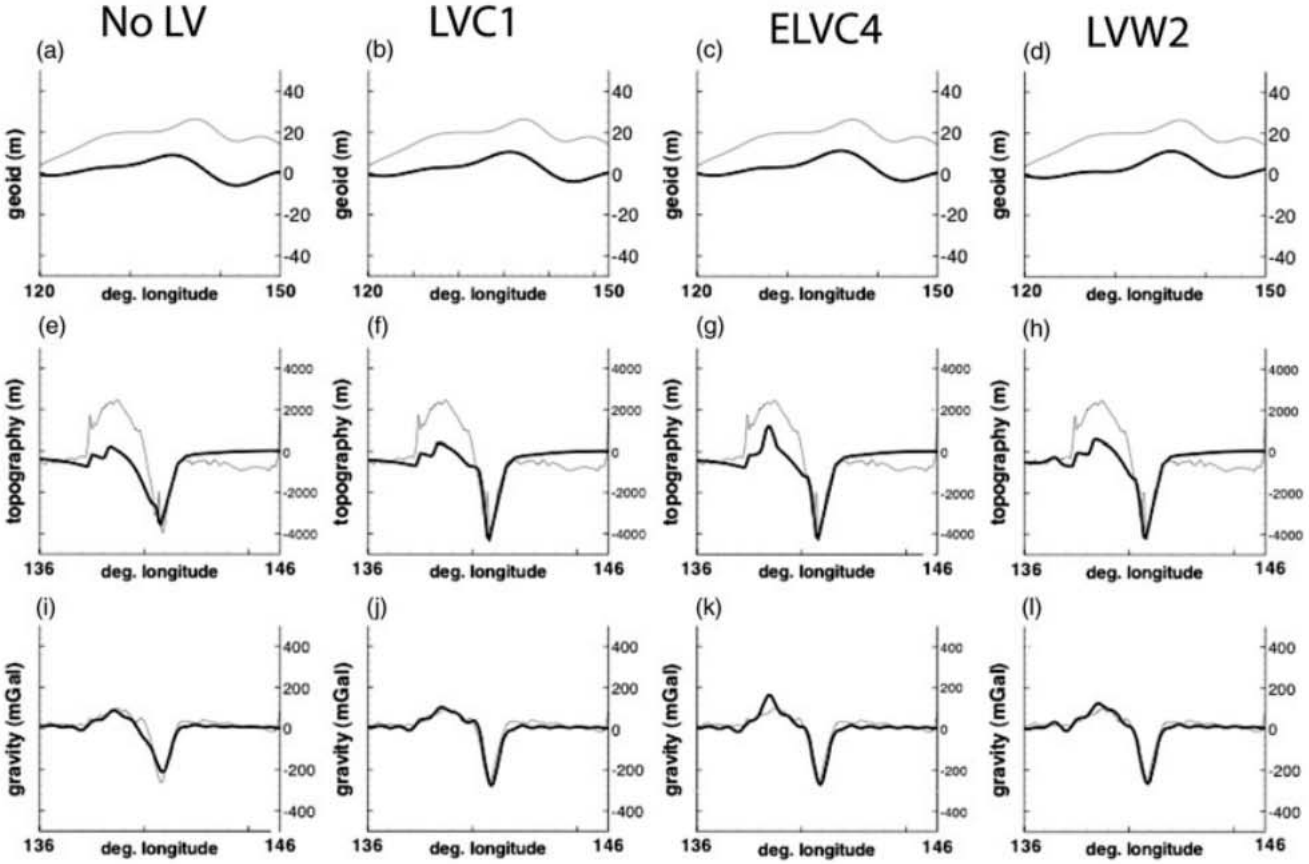

Fig. 5 Results of Northern Izu–Bonin model calculations (Table 1) for geoid height, gravity anomaly, and topography (thick black lines) compared with regional dataset profiles (thin gray lines) for (a,e,i) no low-viscosity (no LV), (b,f,j) LVC1 with 1000 ppm H_2O in olivine as an average value, (c,g,k) ELVC4 with 1000 ppm H_2O in olivine as an average value ($\eta_{LV} = 3.3 \times 10^{19}$–$4.0 \times 10^{20}$ Pa s), and (d,h,l) LVW2 with 1000 ppm H_2O in olivine as an average value. Note that all models shown have zero density contrast between the LV region and the nominally anhydrous mantle wedge. Abbreviations as in Figure 4.

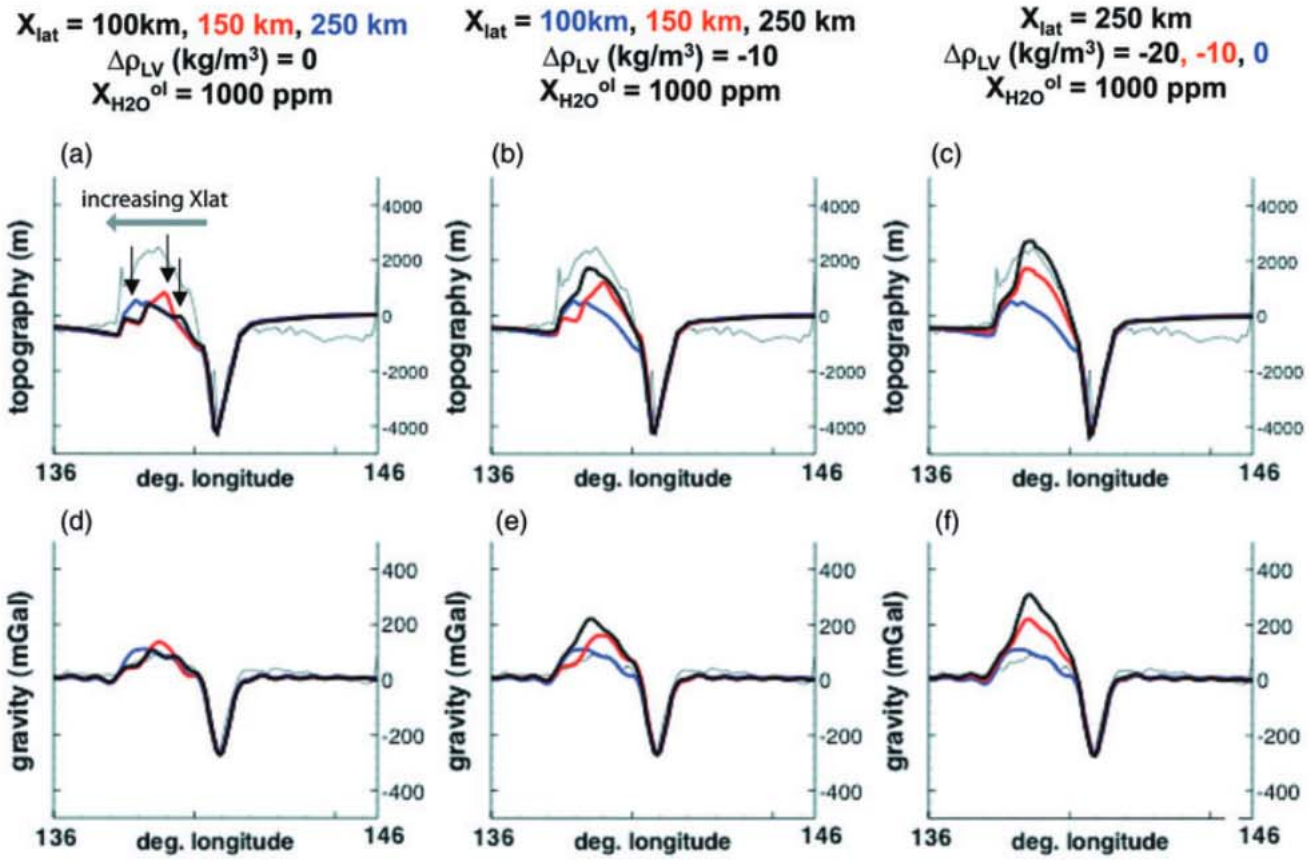

Fig. 6 Independently varying model parameters. (a,b,d,e) Different lateral extents (X_{lat}) of models for the ELVC/LVW, corresponding to the depth of fluid release from the slab. (a,d) ELVC1, 100 km extent (black); ELVC2, 150 km extent (red); ELVC24, 250 km extent (blue), all models have $\Delta\rho = 0$ kg/m^3 between the LV region and the nominally anhydrous mantle wedge, and arrows indicate the changing peak position in the calculated topography. (b,e) ELVC9, 100 km extent (blue); ELVC12, 150 km extent (red); ELVC25, 250 km extent (black), all models have $\Delta\rho = -10$ kg/m^3 between the LV region and the nominally anhydrous mantle wedge. (c,f) Different density contrast between the ambient nominally anhydrous wedge and the ELVC region on calculated topography and gravity anomalies. (c,f) ELVC24, $\Delta\rho = 0$ kg/m^3 (blue); ELVC25, $\Delta\rho = -10$ kg/m^3 (red); ELVC26, $\Delta\rho = -20$ kg/m^3 (black), all models have a lateral LV extent of 250 km. Observed profiles are indicated by thin gray lines in all figure parts. Abbreviations as in Figure 4.

over the relatively narrow (~300 km) Izu–Bonin Arc edifice require a low-viscosity region directly beneath it. Because the maximum width LVW (LVW2, 400 km) does not result in a peaked signal, this calculation can not constrain a maximum depth of fluid release. However, the calculation can be very useful in determining shallower depths of fluid release from the slab, most likely between 100 and 250 km depth and involving dehydration of a lithospheric serpentinite slab source.

Adding, and then changing, the shape of the low-viscosity region (LVC to ELVC) increases trench depth, and more closely predicts the trench depth compared with that observed. Changing the density within the low-viscosity regions to match GyPSM-S output has an additional significant effect on the calculated topography (Fig. 6b,c). Decreasing the density in the ELVC due to water-saturation by 20 kg/m^3 (the lower end of the value predicted by GyPSM-S modeling, Fig. 6c) relative to the ambient nominally anhydrous wedge results in a very close match of the calculated topography and that observed by increasing both the maximum height of the model topography (by ~2.3 km) and the width of the model topography. Decreasing the density by the maximum value (50 kg/m^3) results in a considerable over-prediction of topographic height (by ~3.4 km). Based on the calculated topography, the preferred parameters, which result in a close match to the amplitude and width of the regional dataset as judged by the normalized root mean square (NRMS) deviation (Fig. 7a), involve the horizontal extension of the shallow wedge hydration region to about 200–350 km and include a density contrast within the LV zone of –30 to –10 kg/m^3, which is on the lower end of the range predicted by Billen and Gurnis (2003).

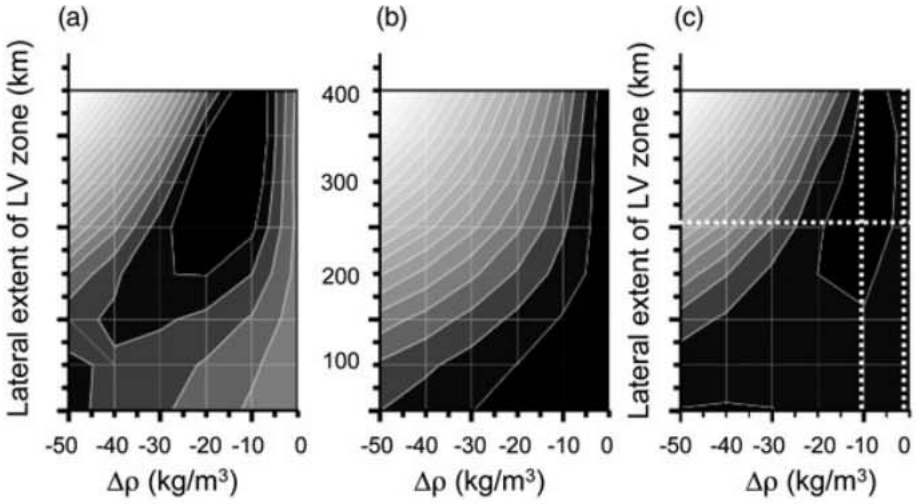

Fig. 7 Comparison of the result of variation of parameters, specifically the density contrast between the LV zone and the nominally anhydrous mantle wedge and the lateral extent of the low viscosity (LV) zone, to the regional profiles for gravity anomalies and topography using RMS error estimates to establish goodness-of-fit (darker colors indicate a better fit). (a) Normalized RMS (NRMS) error calculated for misfit of calculated topography to that observed, (b) NRMS error calculated for misfit of calculated gravity to that observed, and (c) combined NRMS error calculated for the misfit of both gravity and topography, where dotted lines indicate transects in Figure 6.

GRAVITY ANOMALIES AND GEOID HEIGHT

Prediction of the gravity associated with the Izu–Bonin Trench and Arc system, but with no low-viscosity region, results in a slight under-prediction of trench depth, and near-trench variations (Fig. 5i). Similar to the results for topography, introduction of an LVC produces a larger amplitude high near the trench, providing a better match to that observed (LVC1, Fig. 5j), particularly in the forearc region. Lateral extension of the LVC in the shallow wedge below the arc edifice results in an increasing amplitude for the gravity anomaly away from the trench, and significant over-predictions relative to the regional dataset (Figs 5k,6d). However, extension of the low-viscosity region to an LVW geometry, where hydration is produced at depths beyond the arc edifice, provides a better match to that observed (LVW2, Fig. 5l).

Introducing a density variation within the modeled low-viscosity regions results in a similar effect as for the topography, specifically an increase in amplitude (Fig. 6e,f). As the topography in the arc region increases, due to a lessening of the dynamic depression of the arc, the gravity anomaly increases. Varying the density contrast from –50 to 0 kg/m^3 between the low-viscosity region and the ambient mantle wedge in conjunction with the lateral extent of the LV zone shows that the best fit to the regional gravity profile is given by $\Delta\rho = -10$ to 0 kg/m^3 over a range of lateral extents, or an LVC geometry with $\Delta\rho = -30$ to 0 kg/m^3 (Fig. 7b).

Calculation of the model geoid height without a low-viscosity region results in a broad high over the arc and a broad low over the trench, with a similar shape to the observed dataset (Fig. 5a). The amplitudes for the height over both the arc and the trench are larger than that of the regional dataset. Addition of a low-viscosity region increases the amplitude over the arc (Fig. 5b–d), but increasing the relative viscosity contrast by increasing the average water in olivine content has no apparent effect. In fact, besides the initial perturbation seen with the introduction of the LVC from the case lacking any low-viscosity zone, changing geometry of the low-viscosity region does not have a significant effect on the geoid height.

DISCUSSION

DEEP DEHYDRATION AND LV ZONE GEOMETRY

It is apparent from the modeling results in this, and previous (Billen & Gurnis 2001, 2003; Billen *et al.* 2003), studies that the particular geometry of the localized low-viscosity zone is important, and can be reflected in surface observations of geophysical quantities over subduction zones. Previous investigations have alluded to the role of fluids and NAM in producing the hydrated, low-viscosity region (Honda & Saito 2003; Iwamori 2007; Tonegawa *et al.* 2008), or have imposed specific geometries to match regional observations of the dynamic topography, and geoid and gravity anomalies (Billen & Gurnis 2003). Results from coupled geochemical and geodynamic modeling that tracks fluids from sources within the slab through reaction of the fluids with the slab-adjacent wedge material to melt production demonstrates the development of low-viscosity regions

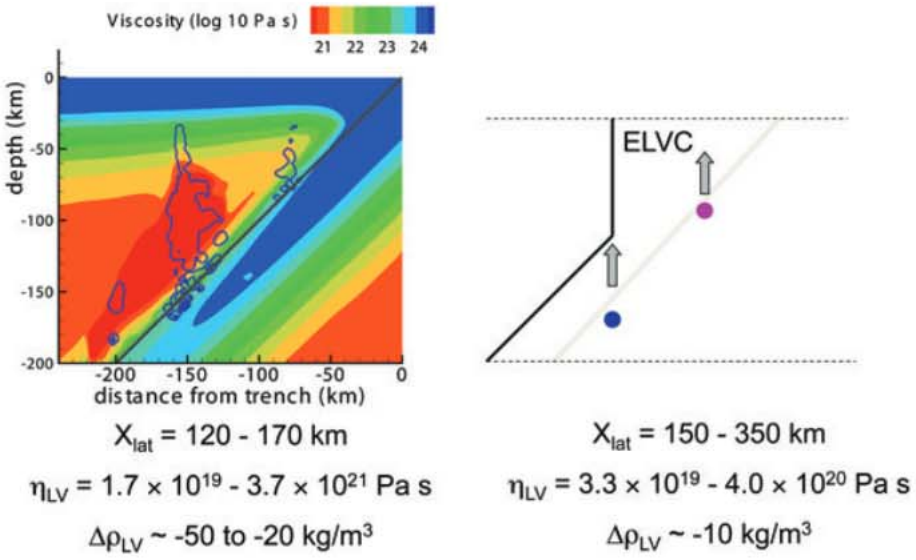

Fig. 8 Comparison of the coupled GyPSM-S northern Izu–Bonin model result (Hebert *et al.* 2009) with the best fit uncoupled result obtained through this study. ELVC, 'extended' low-viscosity channel; X_{lat}, lateral extent of model.

within the wedge and how variations in the geometry of the hydrated regions result from changing subduction parameters such as slab dip, convergence velocity, and slab age, as well as the time-dependence of the hydration process (Hebert *et al.* 2009). We therefore are able to link fundamental aspects in subduction zones such as the depth of fluid transport within the slab, the dehydration pattern, fluid flux, and fluid migration pathways with the resulting size and depth extent of low-viscosity regions within the wedge. This study compares the results of modeling a particular subduction region (NIB) to surface observations of topography, and gravity and geoid anomalies to determine the particular low-viscosity geometry that may exist within the wedge. The strength of the conclusions from the coupled model (Hebert *et al.* 2009) and other studies (Iwamori 2007; Tonegawa *et al.* 2008) are thus tested.

The primary influences on the geometry of the LVC are the fluid release pattern from the slab, which, in turn, depend on the thermal structure of the slab mostly determined by slab age and the slab dip, as steeper dipping slabs lead to narrower regions of fluid infiltration. Slab convergence velocity has a secondary influence on fluid release pattern and is therefore a second-order control on LVC geometry (Hebert *et al.* 2009). According to results from GyPSM-S, more mature slabs, such as seen in the NIB model, allow for shallow fluid releases from the AOC layers within the slab, and a strong, deep fluid release from the serpentinite layer within the slab (Hebert *et al.* 2009). The strong, deep fluid release may result in the time-dependent lengthening of the deep fluid pathway, and, eventually, with vertical fluid transport, an ELVC structure (Hebert *et al.* 2009). The identity of the fluid source is not, however, conclusive. Limitations on the depth extent of the GyPSM-S model domain restrict modeled dehydration to less than 200 km, but it is possible for even deeper dehydration reactions to occur either within the slab serpentinite layer or within hydrous phases stabilized within the hydrated slab-adjacent wedge. Assuming similar fluid pathways, LVW structures with a greater lateral extent may form from even deeper slab fluid sources. It is significant, though, that both Iwamori (2007) and Tonegawa *et al.* (2008) describe vertical migration of aqueous fluid through the mantle wedge originating at depths from 100 to 200 km from dehydration of serpentine and chlorite stabilized within subducting wedge peridotite beneath the Japan arcs, resulting in ELVC-like structures. In NIB, comparison of the observed topography and gravity signals with computed values results in the conclusion that fluid release occurs within the interval 150–350 km depth, forming an ELVC structure with an associated density reduction of about –10 kg/m^3 (Figs 7c,8). This type of low-viscosity structure is in agreement with GyPSM-S results as well as with modeling by Iwamori (2007) and Tonegawa *et al.* (2008) for the Japan arcs.

The results of this study were influenced by the inclusion of the high-viscosity lid, background radial viscosity structure, low-density crustal model, and the higher-density eclogite layer within the slab, but not by the inclusion of the phase

transformations associated with transition zone seismological boundaries. The background values for the transition zone and lower mantle viscosity ($100 \times \eta_0$, $300 \times \eta_0$) are relatively high compared with previous studies (Zhong & Gurnis 1992; Moresi & Gurnis 1996).

We imposed a uniform average value for water content in olivine over the entire low-viscosity region of either 1000 ppm (ELVC4) or 2000 ppm (ELVC5). GyPSM-S calculated water contents in olivine over the shallow water-saturated wedge (< 200 km depth) for the NIB model range 150–1400 ppm, increasing with pressure, and so this average value does not reflect the more complex hydration structure of the wedge and may have an impact on the results. The basis for the compositional part of the viscosity law (Eqn 5) is water in olivine, based on experimental results involving dislocation creep in olivine, and on the assumption of an olivine-dominated rheology, which is appropriate for the mantle. However, a significant fraction of the mantle includes other nominally anhydrous minerals, which can accommodate high water contents (e.g. clinopyroxene with 600–3000 ppm H_2O). Additional water-weakening due to these minerals may be a factor as well, making the high modeled water contents in the shallow wedge not as extreme. Assuming a peridotite assemblage of 57% olivine, 8% garnet, 16% orthopyroxene, and 16% clinopyroxene, the LVC can potentially hold about 2200 ppm H_2O at 200 km depth. We observe a significant influence on the topography with decreasing viscosity within the hydrated zones caused by increasing average water contents in olivine.

COMPARISON WITH OTHER REGIONAL MODELS OF LOW-VISCOSITY ZONES

Evident from the conclusions of Hebert *et al.* (2009), the particular geometry of a regional low-viscosity zone is based on dehydration locations and strength, which is dependent on the thermal structure of the slab, a function of local subduction parameters. The low-viscosity region that allows for a best fit between model data and geophysical observations in the northern Izu–Bonin region corresponds to an ELVC geometry similar to that solved by GyPSM-S (Hebert *et al.* 2009) and to results from other modeling studies in the Japan arcs also involving the Pacific Plate (Iwamori 2007; Tonegawa *et al.* 2008). It is possible to then draw connections between the ultimate depth of a strong fluid source and the lateral extent of the regional low-viscosity zone.

Billen and Gurnis (2003) modeled potential low-viscosity, low-density zones corresponding to two model regions (Tonga–Kermadec, Central Aleutians) with differing subduction parameters. However, the mechanism by which such a zone would form was not directly addressed, and the ultimate geometry of the low-viscosity region was inferred by comparison of regional datasets with computed values for topography and geoid height. Results indicated that both subduction wedges included low-viscosity, low-density regions, but the size of the region and magnitude of the density anomaly within the Tonga–Kermadec subduction zone was greater than that for the Central Aleutians. The primary difference between the two subduction zones is the age of the subducting slab. Tonga–Kermadec involves an older slab (*ca* 105 Ma), while the Central Aleutians involves a significantly younger slab (*ca* 55 Ma) (Syracuse & Abers 2006). Calculations made by Syracuse and Abers (2006) of the depth of the slab beneath the volcanic front (H_9) may indicate that the Central Aleutians involve shallower fluid release (and melting) than Tonga–Kermadec, with H_9 of about 90 and 115 km, respectively. According to results from GyPSM-S modeling, subduction of a more mature slab results in strong, deeper fluid releases, and the possibility for the development of a larger low-viscosity region (Hebert *et al.* 2009). Comparison of model results from Iwamori (2007) for hydration associated with subduction of the hot Philippine Sea Plate with the cooler Pacific Plate also indicate a deepening of fluid release from hydrous phases with subduction of an older slab. These general observations are in agreement with the results from Billen and Gurnis (2003) and indicate that the size and shape of low-viscosity regions within a regional subduction zone wedge can be inferred based on slab age.

CONCLUSIONS

Inclusion of a localized low-viscosity, low-density zone in subduction zone modeling is required in order to match geophysical surface observations. Coupled geochemical and geophysical modeling (GyPSM-S) allows for a fluid-source-based approach to determining a particular low-viscosity geometry based on changing subduction parameters, spatial location of the water-saturated solidus, and the water contents of nominally anhy-

drous minerals. Subsequent modeling of the topography, and gravity and geoid anomalies with inclusion of the particular low-viscosity geometry, can then be performed and compared with observed values. For the N1B system, comparison of the observed topography signal with computed values results in the conclusion that fluid release occurs within the interval at about 150–350 km depth, forming an extended low-viscosity zone (ELVC) with an associated density reduction within the ELVC of about –10 kg/m^3; these values are in general agreement with previous modeling results emphasizing deep dehydration from either subducting lithospheric serpentinite (Hebert *et al.* 2009) or hydrous wedge phases such as serpentine or chlorite (Iwamori 2007; Tonegawa *et al.* 2008).

ACKNOWLEDGEMENTS

The authors thank P. Antoshechkina, P. Asimow, and C. Hall for collaboration with the GyPSM-S modeling effort, and L. DiCaprio and E. Tan for helpful discussions and technical advice. Special thanks to S. Honda and H. Iwamori for very helpful reviews, and to editor Y. Tamura. Support was provided through the Tectonics Observatory by the Gordon and Betty Moore Foundation. This is Contribution Number 106 of the Tectonics Observatory and 10018 of the Division of Geological and Planetary Sciences, California Institute of Technology.

REFERENCES

ARCAY D., TRIC E. & DOIN M.-P. 2005. Numerical simulations of subduction zones: Effect of slab dehydration in the mantle wedge dynamics. *Physics of the Earth and Planetary Interiors* 149, 133–53.

ARKO R., RYAN W., CARBOTTE S. *et al.* 2007. The Global Multi-Resolution Topography (GMRT) Synthesis. Fall Meet. Suppl. Abstract IN51B-0405. *EOS Trans. AGU*, 88(52).

ASIMOW P. D., DIXON J. E. & LANGMUIR C. H. 2004. A hydrous melting and fractionation model for mid-ocean ridge basalts: Application to the Mid-Atlantic Ridge near the Azores. *Geochemistry, Geophysics, Geosystems* 5, Q01E16, doi:10.1029/2003GC000568.

BATCHELOR G. K. 1967. *An Introduction to Fluid Dynamics*. Cambridge University Press, Cambridge.

BELL D. R. & ROSSMAN G. R. 1992. Water in Earth's mantle: The role of nominally anhydrous minerals. *Science* 255, 1391–97.

BILLEN M. I. & GURNIS M. 2001. A low viscosity wedge in subduction zones. *Earth and Planetary Science Letters* 193, 227–36.

BILLEN M. I. & GURNIS M. 2003. Comparison of dynamic flow models for the Central Aleutian and Tonga-Kermadec subduction zones. *Geochemistry, Geophysics, Geosystems* 4, 1035, doi:10.1029/2001GC000295.

BILLEN M. I., GURNIS M. & SIMONS M. 2003. Multiscale dynamics of the Tonga-Kermadec subduction zone. *Geophysical Journal International* 153, 359–88.

BROOKS A. N. & HUGHES T. J. R. 1982. Streamline Upwind Petrov-Galerkin formulations for convection dominated flows with particular emphasis on the incompressible Navier-Stokes equations. *Computer Methods in Applied Mechanics and Engineering* 32, 199–259.

CHRISTENSEN N. I. & MOONEY W. D. 1995. Seismic velocity structure and composition of the continental crust: A global view. *Journal of Geophysical Research* 100, 9761–88, doi:10.1029/95JB00259.

COOPER K. M., EILER J. M., ASIMOW P. D. & LANGMUIR C. H. 2004. Oxygen isotope evidence for the origin of enriched mantle beneath the mid-Atlantic ridge. *Earth and Planetary Science Letters* 220, 297–316.

DAVIES G. F. 1981. Regional compensation of subducted lithosphere: Effects on geoid, gravity and topography from a preliminary model. *Earth and Planetary Science Letters* 54, 431–41.

DAVIES J. H. & STEVENSON D. J. 1991. Physical model of source region of subduction zone volcanics. *Journal of Geophysical Research* 97(B2), 2037–70.

DIXON J. E., LEIST L., LANGMUIR C. H. & SCHILLING J.-G. 2002. Recycled dehydrated lithosphere observed in plume-influenced mid-ocean-ridge basalt. *Nature* 420, 385–9.

DONNELLY K. E., GOLDSTEIN S. L., LANGMUIR C. H. & SPEIGELMAN M. 2004. Origin of enriched ocean ridge basalts and implications for mantle dynamics. *Earth and Planetary Science Letters* 226, 347–66.

FUKAO Y., OBAYASHI M., INOUE H. & NENBAI M. 1992. Subducting slabs stagnant in the mantle transition zone. *Journal of Geophysical Research* 97, 4809–22.

FUKAO Y., WIDIYANTORO S. & OBAYASHI M. 2001. Stagnant slabs in the upper and lower mantle transition region. *Reviews of Geophysics* 39, 291–323.

GAETANI G. A. & GROVE T. L. 2003. Experimental constraints on melt generation in the mantle wedge. *In* Eiler J. (ed.) *Geophysical Monograph*, Vol. 138, pp. 107–34. American Geophysical Union, Washington, DC.

GERYA T. V. & YUEN D. A. 2003. Rayleigh-Taylor instabilities from hydration and melting propel 'cold plumes' at subduction zones. *Earth and Planetary Science Letters* 212, 47–62.

GHIORSO M. S. & SACK R. O. 1995. Chemical mass transfer in magmatic processes; IV, a revised and internally-consistent thermodynamic model for the

interpolation and extrapolation of liquid-solid equilibrium magmatic systems at elevated temperatures and pressures. *Contributions to Mineralogy and Petrology* 119, 197–212.

GORBATOV A. & KENNETT B. L. N. 2003. Joint bulk-sound and shear tomography for Western Pacific subduction zones. *Earth and Planetary Science Letters* 210, 527–43.

GROVE T. L., CHATTERJEE N., PARMAN S. W. & MÉDARD E. 2006. The influence of H_2O on mantle wedge melting. *Earth and Planetary Science Letters* 249, 74–89.

HAGER B. H. 1984. Subducted slabs and the geoid: Constraints on mantle rheology and flow. *Journal of Geophysical Research* 89, 6003–15.

HEBERT L. B., ANTOSHECHKINA P., ASIMOW P., GURNIS M. 2009. Emergence of a low-viscosity channel in subduction zones through the coupling of mantle flow and thermodynamics. *Earth and Planetary Science Letters* 278, 243–56.

HIRTH G. & KOHLSTEDT D. L. 1996. Water in the oceanic upper mantle; implications for rheology, melt extraction, and the evolution of the lithosphere. *Earth and Planetary Science Letters* 144, 93–108.

HONDA S. & SAITO M. 2003. Small-scale convection under the back-arc occurring in the low-viscosity wedge. *Earth and Planetary Science Letters* 216, 703–15.

HONDA S., YOSHIDA T. & AOIKE K. 2007. Spatial and temporal evolution of arc volcanism in the northeast Honshu and Izu-Bonin Arcs: Evidence of small-scale convection under the island arc? *Island Arc* 16, 214–23.

IWAMORI I. 1998. Transportation of H_2O and melting in subduction zones. *Earth and Planetary Science Letters* 160, 65–80.

IWAMORI I. 2007. Transportation of H_2O beneath the Japan arcs and its implications for global water circulation. *Chemical Geology* 239, 182–98.

JEANLOZ R. 1989. High pressure chemistry of the Earth's mantle and core. *In* Peltier W. R. (ed.) *Mantle Convection*, pp. 203–60. Pergamon, New York.

KAWAKATSU H. & WATADA S. 2007. Seismic evidence for deep-water transportation in the mantle. *Science* 316, 1468–71.

KING S. D. 2002. Geoid and topography over subduction zones: The effect of phase transformations. *Journal of Geophysical Research* 107 (B1), 2013, doi:10.1029/2000JB000141.

KING S. D., RAEFSKY A. & HAGER B. H. 1990. ConMan; vectorizing a finite element code for incompressible two-dimensional convection in the Earth's mantle. *Physics of the Earth and Planetary Interiors* 59, 195–207.

KITAMURA K., ISHIKAWA M. & ARIMA M. 2003. Petrological model of the northern Izu-Bonin-Mariana arc crust: Constraints from high-pressure measurements of elastic wave velocities of the Tanzawa plutonic rocks, central Japan. *Tectonophysics* 371, 213–21.

LE ROUX P. J., LE ROUX A. P., SCHILLING J. G., SHIMIZU N., PERKINS W. W. & PEARCE N. J. G. 2002. Mantle heterogeneity beneath the southern Mid-Atlantic Ridge: Trace element evidence for contamination of ambient asthenospheric mantle. *Earth and Planetary Science Letters* 203, 479–98.

LEMOINE F. G., KENYON S. C., FACTOR J. K. *et al.* 1998. *The Development of the Joint NASA GSFC and NIMA Geopotential Model EGM96*. NASA Goddard Space Flight Center, Greenbelt, MD.

MANEA V. & GURNIS M. 2007. Subduction zone evolution and low viscosity wedges and channels. *Earth and Planetary Science Letters* 264, 22–45.

MORESI L. & GURNIS M. 1996. Constraints of the lateral strength of slabs from three-dimensional dynamic flow models. *Earth and Planetary Science Letters* 138, 15–28.

MÜLLER R. D., ROEST W. R., ROYER J.-Y., GAHAGAN L. M. & SCLATER J. G. 1997. Digital isochrons of the world's ocean floor. *Journal of Geophysical Research* 102, 3211–14.

PRIBAC F. 1991. *Superswells due to Mantle Convection*. PhD thesis. Australian National University, Canberra.

SANDWELL D. T. & SMITH W. H. F. 1997. Marine gravity from Geosat and ERS-1 altimetry. *Journal of Geophysical Research* 102, 10 039–54.

SCHMIDT M. W. & POLI S. 1998. Experimentally based water budgets for dehydrating slabs and consequences for arc magma generation. *Earth and Planetary Science Letters* 163, 361–79.

SCHROEDER W. 1984. The empirical age-depth relation and depth anomalies in the Pacific Ocean Basin. *Journal of Geophysical Research* 89, 9873–83.

SLEEP N. H. 1975. Stress and flow beneath island arcs. *Geophysical Journal International* 42, 827–57.

SMITH P. M. & ASIMOW P. D. 2005. Adiabat_1ph: A new public front-end to the MELTS, pMELTS, and pHMELTS models. *Geochemistry, Geophysics, Geosystems* 6(2), Q02004, doi:10.1029/2004GC000816.

STERN R. J., FOUCH M. J. & KLEMPERER S. L. 2003. An overview of the Izu-Bonin-Mariana subduction factory. *In* Eiler J. (ed.) *Geophysical Monograph* 138, 175–222.

SUYEHIRO K., TAKAHASHI N. & ARIIE Y. *et al.* 1996. Continental crust, crustal underplating, and low-Q upper mantle beneath an oceanic island arc. *Science* 272, 390–2.

SYRACUSE E. M. & ABERS G. A. 2006. Global compilation of variations in slab depth beneath arc volcanoes and implications. *Geochemistry, Geophysics, Geosystems* 7, Q05017, doi:10.1029/2005GC001045.

TAKAHASHI N., KODAIRA S., KLEMPERER S. L., TATSUMI Y., KANEDA Y. & SUYEHIRO K. 2007. Crustal structure and evolution of the Mariana intra-oceanic island arc. *Geology* 35, 203–6.

TAKAHASHI N., SUYEHIRO K. & SHINOHARA M. 1998. Implications from the seismic crustal structure of the northern Izu-Bonin arc. *Island Arc* **7**, 383–94.

TONEGAWA T., HIRAHARA K., SHIBUTANI T., IWAMORI H., KANAMORI H. & SHIOMI K. 2008. Water flow to the mantle transition zone inferred from a receiver function image of the Pacific slab. *Earth and Planetary Science Letters* **274**, 346–54.

VAN DER HILST R. D., ENGDAHL R., SPAKMAN W. & NOLET G. 1991. Tomographic imaging of subducted lithosphere below northwest Pacific island arcs. *Nature* **353**, 37–43.

WIDIYANTORO S., KENNETT B. L. N. & VAN DER HILST R. D. 1999. Seismic tomography with P and S data reveals lateral variations in the rigidity of deep slabs. *Earth and Planetary Science Letters* **173**, 91–100.

ZHONG S. & GURNIS M. 1994. Controls on trench topography from dynamic models of subducted slabs. *Journal of Geophysical Research* **99**(B8), 15 683–95.

ZHONG S. & GURNIS M. 1992. Viscous flow model of a subduction zone with a faulted lithosphere: Long and short wavelength topography, gravity and geoid. *Geophysical Research Letters* **19**, 1891–4.

ZHONG S., GURNIS M. & HULBERT G. M. 1993. Accurate determination of surface normal stress in viscous flow from a consistent boundary flux method. *Physics of the Earth and Planetary Interiors* **78**, 1–8.

ZHONG S., GURNIS M. & MORESI L. 1998. Role of faults, nonlinear rheology, and viscosity structure in generating plates from instantaneous mantle flow models. *Journal of Geophysical Research* **103**, 15 255–68.